

# Persistence of symmetry-protected Dirac points at the surface of the topological crystalline insulator SnTe

Olga Arroyo-Gascón<sup>1,\*</sup>, Yuriko Baba<sup>2</sup>, Jorge I. Cerdá<sup>1,†</sup>, Oscar de Abril<sup>3</sup>,

Ruth Martínez<sup>2</sup>, Francisco Domínguez-Adame<sup>2</sup> and Leonor Chico<sup>2,1</sup>

<sup>1</sup> *Instituto de Ciencia de Materiales de Madrid, Consejo Superior de Investigaciones Científicas, C/ Sor Juana Inés de la Cruz 3, E-28049 Madrid, Spain*

<sup>2</sup> *GISC, Departamento de Física de Materiales, Universidad Complutense, E-28040 Madrid, Spain and*

<sup>3</sup> *Departamento de Estructuras y Física de Edificación, Universidad Politécnica de Madrid, E-28031 Madrid, Spain*

(Dated: August 17, 2021)

We investigate the effect of a non-magnetic donor impurity located at the surface of the SnTe topological crystalline insulator. Both, semi-infinite and slab geometries are considered. We analyze the changes on the surface states due to the impurity by means of *ab-initio* simulations of the electronic structure of pristine and impurity-doped SnTe. Furthermore, both minimal and Green's function continuum models are proposed in order to describe the effect of the impurity on the surface states. We find that the Dirac cones are shifted down in energy upon doping; this shift depends on the position of the impurity with respect to the surface. We compare slab and semi-infinite geometries within the *ab-initio* approach, demonstrating that the surface states are gapless in the doped semi-infinite system. The gap opens in the slab geometry due to hybridization of the states at opposite surfaces. Finally, by means of a continuum model, we extrapolate our results to arbitrary positions of the impurity, clearly showing a non-monotonic behavior of the Dirac cone.

## I. INTRODUCTION

The discovery of topological insulators in the past decade has fueled great interest in Dirac matter. These materials are insulating in the bulk, but host protected electronic states in their boundaries; namely, surface or edge modes in the three-dimensional or two-dimensional case, respectively [1, 2]. Such gapless boundary states are protected by time-reversal-symmetry (TRS); they have a Dirac spectrum and show spin-momentum locking, a promising property for their application in spintronic devices and quantum information processing [3]. TIs are successfully characterized by the  $\mathbb{Z}_2$  topological invariant, which is related to the number of gapless Kramers pairs in their boundaries; in fact, they show an odd number of Dirac cones at their surfaces. The discovery of topological insulators has led to the recognition that symmetry-protected topological (SPT) phases of matter are more abundant and ubiquitous than expected [4].

One of the families within the broad class of SPT matter are topological crystalline insulators (TCIs). Unlike  $\mathbb{Z}_2$  insulators, TCIs are protected by crystal symmetries and present an even number of Dirac cones in their surfaces, so that their  $\mathbb{Z}_2$  index is zero. These symmetries include rotations, reflections, or even glide planes. The first TCIs discovered were IV-VI semiconductors, such as SnTe and  $\text{Pb}_{1-x}\text{Sn}_x\text{Te}$  ternary alloys, which are protected by mirror symmetries [5–8]. When a mirror symmetry is responsible for the topological protection, the relevant topological invariant is the mirror Chern number  $n_M$ .

SnTe has a rocksalt crystalline structure with small bandgaps at the  $L$  points of the Brillouin zone (BZ), where the conduction and valence bands, which are mainly derived from  $p$  orbitals, are inverted due to the non-negligible SOC [5]. The mirror plane that protects these topological states is  $\{110\}$ , so that an even number of robust Dirac cones appear at the  $\{001\}$ ,  $\{110\}$  and  $\{111\}$  crystal surfaces, which are symmetric with respect to the  $\{110\}$  mirror reflection. For the  $[001]$  surface termination, equivalent  $L$  points of the BZ are projected in the  $\Gamma L_1 L_2$  plane. Hybridization gives rise to two pairs of Dirac cones, deviated from the high-symmetry point  $\bar{X}$  (see Figure 1(d)). SnTe undergoes a crystalline phase transition at low temperatures (below 100 K) to a rhombohedral lattice. Such distortion has a small effect in the bulk bands, but destroys the surface Dirac cones, as any other perturbation that breaks the mirror  $\{110\}$  symmetry would do [9]. Interestingly, within this rhombohedral phase, SnTe has been recently shown to be a higher-order topological insulator, showing hinge states along specific directions [10].

On the other hand, PbTe, which also has a rocksalt structure, is not a TCI and its surfaces are gapped. Notwithstanding, a topological phase transition can be induced either by pressure or alloying. In particular, as anticipated above,  $\text{Pb}_{1-x}\text{Sn}_x\text{Te}$  is a topologically non-trivial material ( $n_M = -2$ ) for  $x \gtrsim 1/3$  [6, 8]. Actually, a band inversion as a function of the alloy composition was reported long time ago [11].

Thin films of these TCIs also show nontrivial topological behavior; however, hybridization effects between the surface states open a gap that decays for increasing layer thickness [12, 13]. In fact, a non monotonic damped oscillation has been found, that is ultimately related to the alternation between nonsymmorphic and

\* o.arroyo.gascon@csic.es

† Deceased.

symmorphic symmetry with the number of atomic layers [12, 14]. Specifically, if a [001]-oriented SnTe slab has an even number of layers, it possesses a nonsymmorphic symmetry. This reduces the hybridization between surface states, whereas for an odd number of layers the symmetry is symmorphic, and more sizeable band gaps appear.

Additionally, symmetry-protected surface states in TCIs can be tuned by introducing impurities. The effects of doping on the electronic structure of bulk SnTe have been addressed in [15, 16]. As for the [001] surface, In doping [17] and diluted impurities [18] have been considered. Impurities in TCI thin films may open a gap or modify the surface states, allowing for the control of topological phase transitions in these materials and constituting an additional tool to modulate their properties [19, 20].

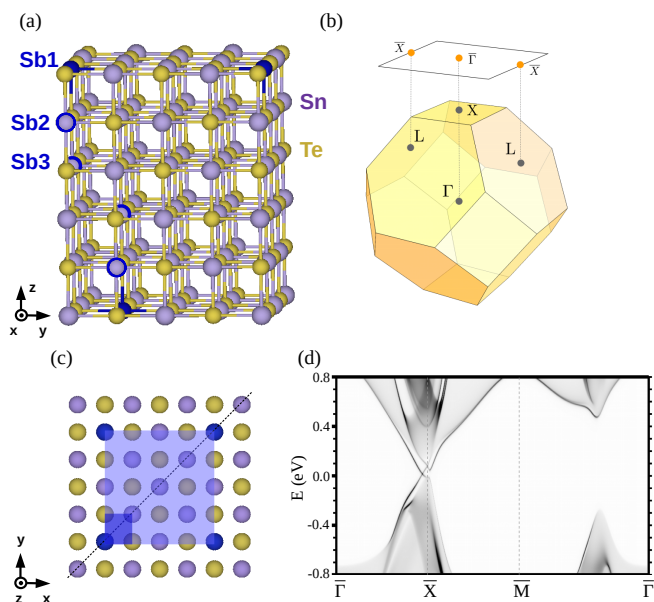


FIG. 1. (a) SnTe 6-atomic-layer slab unit cell. Sb impurities are highlighted in blue: in the Sb1 case, the whole atoms are colored; in the Sb2 and Sb3 case, the impurity atoms are circled. (b) Face-centered cubic Brillouin zone and projected (001) plane. (c) Top view of the  $c(4 \times 4)$  (light blue) and  $1 \times 1$  (dark blue) unit cells. The mirror symmetry plane is represented by a dotted line. (d) SnTe [001] surface band structure of the semi-infinite system.

In this work, the effect of non-magnetic impurities in the topological crystalline insulator SnTe is studied. Specifically, we consider Sn substitution by a Sb atom, which acts as a donor impurity. In fact, Sb-doped SnTe has been found to be a superconductor [21]. Here, we focus on the changes in the TCI dispersion relations induced by the presence of the Sb impurity. To this end, DFT-based *ab-initio* simulations are used to characterize SnTe and the effect of the non-magnetic donor impurity near the crystal surface. We address the hybridization

between surface and impurity states as well as the effect of the impurity position on the electronic structure and crystal symmetries. Furthermore, both perturbation theory and Green's function models are proposed. The former is used to predict the behavior of the Dirac cone upon doping, while the latter describes the impurity states.

## II. FIRST-PRINCIPLES APPROACH

### A. Geometry and methods

Our calculations were performed using the pseudopotential DFT SIESTA code [22] with the generalized gradient approximation under the PBE parametrization (GGA-PBE) for the exchange and correlation functional [23]. Spin-orbit coupling (SOC) was considered within the fully-relativistic pseudopotential formalism [24] for all calculations unless otherwise stated. Accordingly, a relativistic pseudopotential was employed, following the Troullier-Martins method.

A double- $\zeta$  singly-polarized basis set was chosen for all the atoms involved, with a radial extension of the strictly localized orbitals determined from a confinement energy (energy shift) of 100 meV. The resolution of the real space grids was set to around  $0.06 \text{ \AA}^3$  (equivalent to a mesh cutoff of 600 Ry). For the integration over the BZ we employed  $k$ -supercells of around  $(17 \times 17)$  relative to the SnTe- $(1 \times 1)$  bulk unit cell, with a temperature in the Fermi-Dirac occupation function of 100 meV.

A lattice parameter of  $6.39 \text{ \AA}$  was used following Refs. [5, 15] which yields a satisfactory agreement to experimental results and a successful reproduction of the band gap [11]. This allows us to model rocksalt room-temperature SnTe, avoiding the aforementioned rhombohedral phase transition [8]. In order to tackle the robustness of the surface states against film thickness, several slab calculations were performed using different number of layers (not shown here); we found an optimal compromise between accuracy and our computational capability for a nonsymmorphic 16 atomic-layer SnTe slab. Therefore, all the slab calculations presented in this work have been calculated for this thickness.

Substitutional donor impurities have been considered by replacing an Sn atom by Sb within a  $c(4 \times 4)$  supercell—that is, in a defected layer one out of eight Sn atoms is substituted by an Sb. We have considered up to four different locations of the Sb: at the top surface layer (Sb1), the second (Sb2), third (Sb3) and fourth (Sb4). Furthermore, in order to avoid net dipoles in the slab, another Sb substitutional impurity was always placed at an equivalent position, but with respect to the bottom layer (see Figure 1(a)), so that both are at the same distance from the corresponding nearest surface and the simulated impurity doping in the slabs corresponds to a small value of  $x = 0.016$ .

Atomic relaxations were performed for each structure:

for the Sb1 slab, the three top and bottom layers were relaxed while for the Sb2, Sb3 and Sb4 slabs, the 3, 4 and 5 layers counted from the top and bottom surfaces were included in the relaxations until forces on the atoms were below  $0.02 \text{ eV}/\text{\AA}$ . The top and bottom layers of the final equilibrium structure is the most affected by the relaxation; the Sb1 and Sb3 slabs are displaced up to  $0.17 \text{ \AA}$  compared to  $0.14 \text{ \AA}$  for the Sb2 and Sb4 slabs.

Although minimal, the hybridization of opposite surface states still has an effect on the band structure. Hence, the electronic and spin structure of the Sb-doped SnTe(001) surface will be mainly presented as calculated under a semi-infinite geometry via projected density of states and magnetization maps,  $\text{PDOS}(k, E)$  and  $M_{x/y/z}(k, E)$ , respectively. [25, 26]. To this end we employed surface Green's function matching techniques in order to couple the Hamiltonian matrix elements of the top half of the slab with those of a bulk SnTe calculation. Self-consistency was preserved in the matching process, as reflected by the fact that maximum deviations are always smaller than  $10 \text{ meV}$  between the on-site energies of the Sn and Te central layers of the slab and those in the SnTe bulk. PDOS and  $M_\alpha(k, E)$  maps were computed with a resolution of  $0.003 \text{ \AA}^{-1}$  in reciprocal space and  $5 \text{ meV}$  in energy. Accordingly, the self-energy that determines the spectral width of any surface states (imaginary part of the energy entering the Green's function) was set to  $5 \text{ meV}$ . For zoom ins of the Dirac points we computed additional maps with an increased resolution ( $0.0016 \text{ \AA}^{-1}$  and  $3 \text{ meV}$ ) around the  $\bar{\Gamma}$ -point and over a small energy window. In the semi-infinite calculations, a single impurity is used. For topologically-protected surface states, we expect them to remain unaltered, since the placement of a single impurity does not change the  $\{110\}$  mirror symmetry. On the contrary, the 16 atomic layer slabs do break this symmetry by taking into account two impurities. Since two-dimensional (few-layer) topological crystalline insulators are also the subject of great attention, we consider this comparison to be relevant.

### B. Ab-initio results

Top panel of Figure 2 displays the effect of the substitutional Sb on the surface electronic structure for the four locations of the impurity, Sb1 to Sb4, as it is moved from the surface layer towards the bulk. The band structures have been computed along the  $\bar{\Gamma} - \bar{X}$  direction for 16-layer slabs (that is, under an ultrathin film geometry). Note that, due to band folding, the  $\bar{X}$  point in the  $(1 \times 1)$  BZ back folds into the  $\bar{\Gamma}$  point of the supercell's BZ. For the sake of comparison, we also include in the left column the  $k$ -folded SnTe pristine surface computed under the same  $c(4 \times 4)$  supercell as that used for the defected structures. There are several features immediately apparent in the plots. First of all, in all defected surfaces the Sb develops a split impurity band that disperses across the gap. Interestingly, the band is more lo-

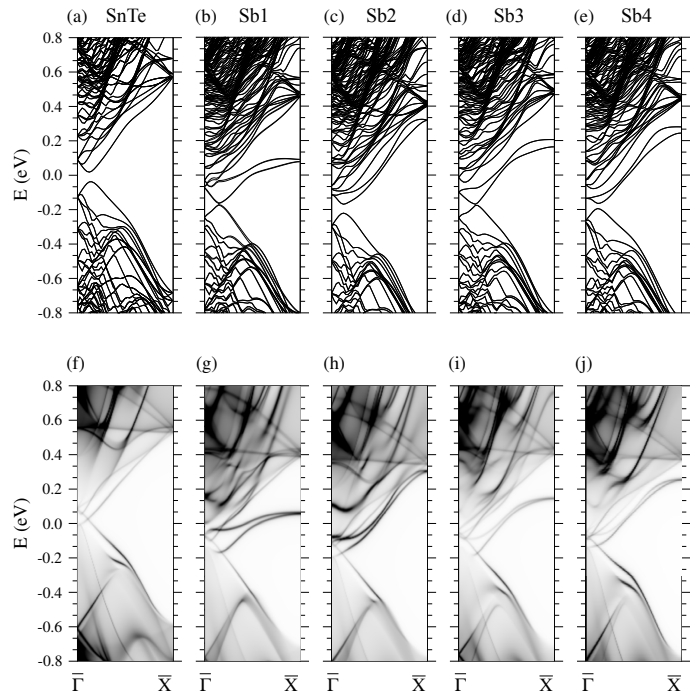


FIG. 2. Electronic structure of pristine SnTe (left column) and Sb-doped SnTe, with the donor impurity located in the first, second, third and fourth atomic layer. Top panel: band structures of the 16-layer slab. Bottom panel: projected density of states  $\text{PDOS}(\mathbf{k}, E)$  on the first atomic layers for the semi-infinite system.

calized when the impurity is located at an odd-numbered layer (particularly the Sb1 case but also Sb3), whereas if located at an even-numbered layer (Sb2 and Sb4 cases) it becomes more dispersive and runs closer to the edge of the bulk conduction band (CB). Second, the presence of the impurity induces a clear  $n$ -type doping as the Fermi level  $E_F$  shifts towards the CB minimum in all defected structures, while it is pinned just above the valence band (VB) maximum for the pristine surface. This doping effect will be further addressed in Sec. III using a minimal continuum model. Third, the Dirac cones slightly away from  $\bar{\Gamma}$  remarkably persist in all defected cases. However, despite the large thickness of the slabs employed, all DPs present a gap due to the long decay length of the topological surface states, so that there is still a sizeable interaction between the top and bottom surfaces. The size of this gap is minimal for the odd cases (Sb1 and Sb3), while it attains values of around  $10 \text{ meV}$  for the even cases (Sb2 and Sb4) and for the pristine surface. Moreover, the breaking of the  $\{110\}$  mirror symmetry in the two-impurity geometry used in the slabs affects the symmetry-protected surface states and contributes to the gap opening, as depicted in panels (b)-(e). Although such even-odd behavior in the Dirac cone (DC) gap value with the impurity position is reminiscent of the nonsymmorphic-symmorphic effect with respect to the

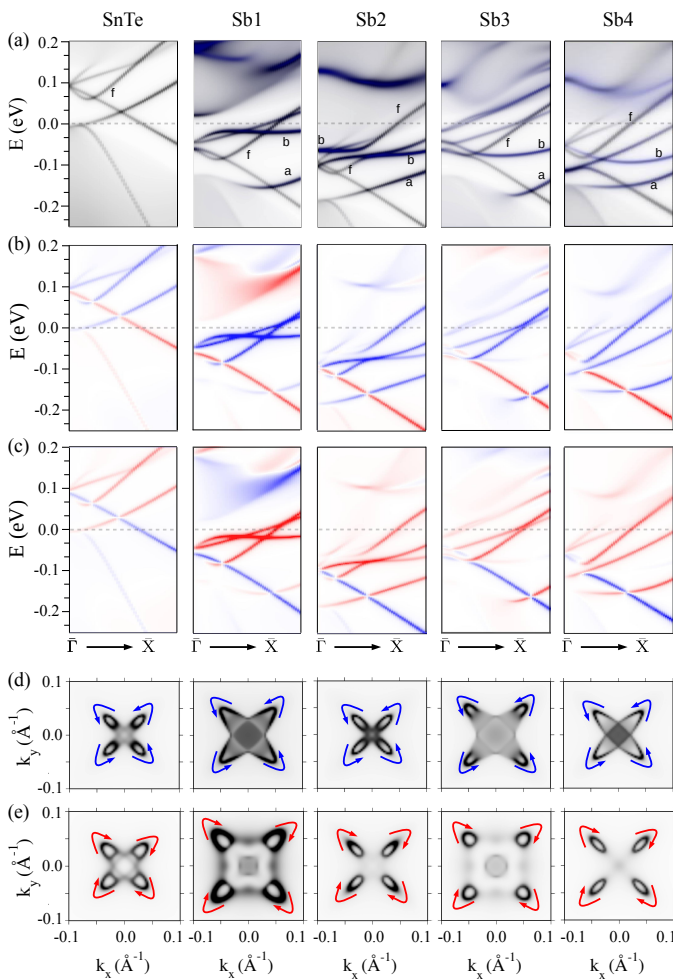


FIG. 3. Zoomed PDOS( $\mathbf{k}, E$ ) (a) and  $M_{x/y}$  (b,c) maps of the semi-infinite structure. In panel (a), the Sb impurity contribution is highlighted in blue. (d) PDOS( $k_x, k_y$ ) maps at 20 meV below the Dirac point. (e) PDOS( $k_x, k_y$ ) maps at 20 meV above the Dirac point. The spin textures are depicted with arrows that outline the spin direction.

number of layers previously reported [12, 14], we note that in our case its origin should be different, because all slabs are composed of the same number of layers.

The bottom panel of Figure 2 displays the equivalent electronic structures to the top panel but in the form of PDOS( $k, E$ ) maps, since they have been computed under a semi-infinite geometry (see previous section). The Sb-doped surfaces, overall, show a similar behavior to that found for the 16-layer slabs, namely: the appearance of Sb impurity bands across the gap showing an even-odd effect in their dispersion, a clear  $n$ -type doping and the presence of DCs slightly away from  $\bar{\Gamma}$ . The SOC-induced splitting of the impurity bands remains small until it approaches the  $\bar{\Gamma}$  point, where the two branches start to deviate from each other by more than 100 meV.

Focusing now on the electronic structure around the  $\bar{\Gamma}$  point, the most relevant feature is the survival of the sur-

vival of a gapless Dirac point (DP) in all structures, which is consistent with the fact that the  $\{110\}$  mirror plane still holds in the doped structures and, hence, the DPs remain symmetry-protected. However, there are qualitative differences with respect to the pristine surface which are best seen in Fig. 3, where zoom ins with an enhanced resolution are presented. First of all, and in accordance with the  $n$ -type doping mentioned above, the DPs consistently shift by around 150–200 meV towards lower energies. Precisely at the  $\bar{\Gamma}$  point the interpretation of the electronic structure becomes more complex due to the profusion of extra bands arising from both the Sb impurity and the band folding.

All relevant bands within the gap are better resolved in Fig. 3(a), where we present zooms of the PDOS( $k, E$ ) maps. The projections have been taken over the surfacemost SnTe layer superimposing the Sb contributions in blue (recall that for the Sb1 case the formula unit at the layer is  $\text{Sn}_7\text{SbTe}_8$ ). For the clean surface case, the branches forming the DC can be clearly identified, as well as the Sb-split impurity bands, denoted as  $a$  and  $b$ . There is a further band inside the gap, labeled by  $f$ , corresponding to the back-folded topological surface state (TSS) along  $\bar{\Gamma} - \bar{M}$  (see Fig. 1(d)). In the lower panels (b) and (c), magnetization maps along the  $x$ - and  $y$ -axis,  $M_{x/y}(k, E)$ , respectively, are shown (we omit the out-of-plane component  $M_z$  since it is always negligible except for Sb1). As could be expected, the in-plane spin orientation of this band remains unaltered with respect to the pristine case. Indeed, this is best seen in the PDOS( $k_x, k_y$ ) maps shown in the lower panels, computed at energies 20 meV below (panel (d)) and above (panel (e)) the location of the DP.

The spin texture for all structures is shown in Fig. 4 in the form of  $M_{x/y}(k, E)$  maps. Note that pristine SnTe only shows in-plane spin polarization due to time-reversal and mirror symmetries [27]. The effect of folding on the spin texture of pristine SnTe is explicitly detailed in the Appendix (Fig. A.1), as well as in additional  $M_{x/y}(k_x, k_y)$  maps near the DP for all structures (Fig. A.2). Close inspection of the spin textures reveals that the spin orientation of the TSSs always remains unchanged with respect to the pristine surface. More surprising is the behavior of the Sb bands; close to  $\bar{X}$  they behave as standard Rashba split states, with a reduced separation in energy between  $a$  and  $b$  of only 10–20 meV while they present opposite magnetizations (in fact, this is the only region where out-of-plane magnetization,  $M_z$ , is not negligible).

Being such ultrathin layers, the energy shift of the DP can be related to quantum size effects. In order to clarify this point, we study the spatial distribution of the wavefunction for the impurity band, depicted in Fig. 5. A series of nodes appear right after the impurity and approximately each two atomic layers in the  $z$ -direction. When the impurity is located at an odd atomic layer, there is an even number of layers above it, so the wavefunction amplitude is almost zero at the surface layer. In contrast,



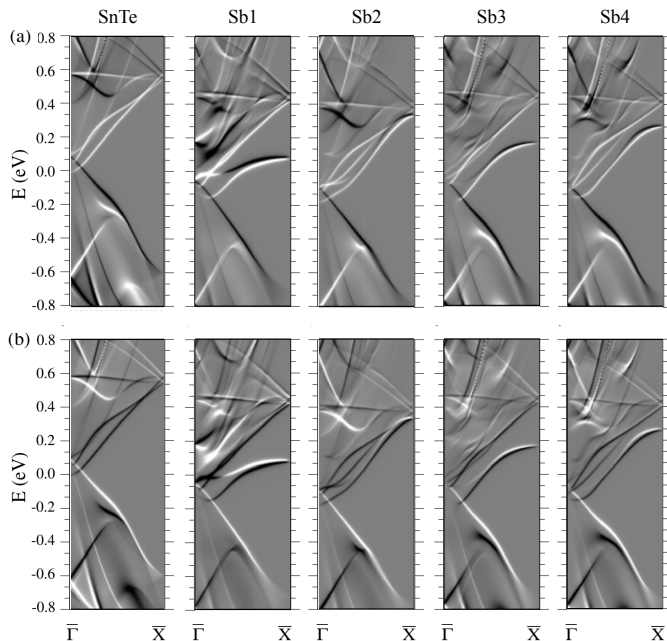


FIG. 4. Magnetization maps  $M_x(k, E)$  (a) and  $M_y(k, E)$  (b) for the semi-infinite pristine and Sb-doped structure, projected on the first atomic layers. White and black shades account for positive and negative values of  $M_i$ , respectively.

when the impurity is placed in an even layer, there is an odd number of layers above it and the wavefunction is nonzero at the surface, therefore favoring hybridization with the surface states and a larger band gap. Since the derivative of the wavefunction is related to the kinetic energy operator, it is also expected for these impurity bands to move upwards, as shown in both slab and semi-infinite calculations in Fig. 2. Thus, we conclude that this energy shift can be also seen as a size or confinement effect.

### III. CONTINUUM MODEL

In order to have an insight into the effect of the impurity upon the Dirac cones and the behavior of the impurity band when the position of the donor Sb atom is varied, we resort to a simple continuum model of a TI. It consists of an isotropic four-band continuum Hamiltonian in a particle-hole symmetric scenario. In fact, this model has been already employed for TIs [28, 29]. The Hamiltonian in momentum space is given by (we set  $\hbar = 1$  hereafter)

$$\mathcal{H}_0 = \epsilon \mathbb{1}_4 + v \boldsymbol{\alpha} \cdot \mathbf{k} + (m - Bk^2) \beta, \quad (1)$$

where  $\epsilon$  is a constant energy term,  $\mathbb{1}_4$  is the  $4 \times 4$  identity matrix,  $v$  is the Fermi velocity,  $m$  is the mass parameter related to the gap and the constant  $B$  takes into account the quadratic terms in momentum. In the former expression,  $\boldsymbol{\alpha}$  and  $\mathbf{k}$  are, respectively, the vector

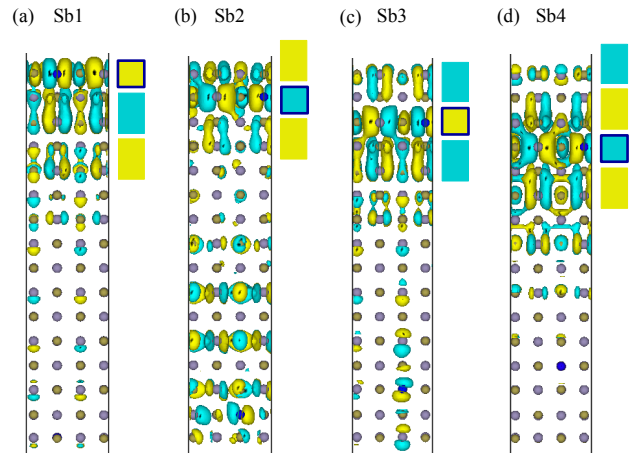


FIG. 5. Wavefunctions for one of the impurity bands at  $\bar{\Gamma}$ . Yellow and blue colors represent positive and negative values, respectively. The colored rectangles next to each panel, which are two atomic layers wide, outline the alternation of regions with positive and negative values of the wavefunction in the  $z$ -direction. The layer where the impurity is located is highlighted in dark blue.

of Dirac matrices and the momentum-vector defined as  $\boldsymbol{\alpha} = (\alpha_x, \alpha_y, \alpha_z)$  and  $\mathbf{k} = (k_x, k_y, k_z)$ . We choose the Dirac matrices expressed in terms of the Pauli matrices in the following basis:  $\alpha_i \equiv \sigma_x \otimes \sigma_i$ ,  $\beta \equiv \sigma_z \otimes \sigma_0$ . This simple model has the minimum elements needed to show topologically protected surface states if  $mB > 0$  and the translational symmetry is broken by making a finite-size system [30].

Modifications of this model, including anisotropy and on-site momentum dependent terms, have been successfully proposed to study the  $\text{Bi}_2\text{Se}_3$  family of materials [29, 31]. In fact, the model has also been applied to describe the [001] surface states of SnTe including just the leading terms linear in momentum [5, 12, 14, 27, 32, 33]. Since our first goal within the continuum approach is to analyze the effect of an impurity in an isolated surface, quadratic terms are indispensable to have a nontrivial topology in a vacuum-SnTe heterojunction [28]. We expect to find the same shifting behavior as predicted by [14] and our DFT calculations. Thus, we perform first-order perturbation theory (PT) on the surface states obtained within this formalism with the aim of elucidating the effect of the impurity on the gapless surface states. Secondly, in order to describe the energy dependence of the impurity states with respect to the impurity position, we solve a simplified version of the Hamiltonian presented in Eq. (1), summing up all terms in the perturbation series using a Green's function method. These two approaches allow us to investigate complementary aspects of the problem.

### A. Perturbation theory approach

With the aim of comparing PT results with DFT calculations, we consider the case of a semi-infinite system which extends from  $z > 0$ , being infinite in the other perpendicular directions. The surface states are derived in Appendix B imposing Dirichlet boundary conditions at the plane  $z = 0$ ; in this way we obtain two Kramers partners that only differ for the spinorial part  $\Phi_{\pm}^0$ :

$$\psi_{\pm} = A_s(e^{-\lambda_1 z} - e^{-\lambda_2 z}) \exp[i(k_x x + k_y y)] \Phi_{\pm}^0. \quad (2)$$

In the former expression, the inverses of the decay are given by  $\lambda_1$  and  $\lambda_2$ , which are functions of the in-plane momenta [see Eq. (B2)], and  $A_s$  is a normalization factor (see Appendix B). The dispersion of the states is linear in the in-plane momenta, yielding the Dirac cones of the surface states inside the bulk gap:  $E_{\pm} = \epsilon \pm v k_{\parallel} \text{sign}(B)$ , where  $k_{\parallel} = \sqrt{k_x^2 + k_y^2}$ .

For the purpose of obtaining the corrections on the energy, we perform first-order perturbation theory modeling the impurity with a Coulomb-like interaction:

$$\Delta \mathcal{H} = -\frac{2R_y^* a_B^*}{\sqrt{(z - z_0)^2 + x^2 + y^2}}, \quad (3)$$

where  $z_0$  is the depth where the impurity is located, and  $R_y^*$  and  $a_B^*$  are the effective Rydberg energy and Bohr radius inside SnTe [34, 35]. The former constants provide the correct units to the expression and scale the interaction due to the medium (see Eq. (B6)).

The first-order correction in perturbation theory is given by

$$\Delta E_{\pm}^{(1)} = \langle \psi_{\pm} | \Delta \mathcal{H}_0 | \psi_{\pm} \rangle, \quad (4)$$

where  $\psi_{\pm}$  are the surface states as defined in Eq. (2) for the impurity-free case. Due to the trivial structure of the correction in the spin space, both states,  $\psi_+$  and  $\psi_-$ , show the same correction. Therefore, the cones are just shifted by the same amount and no gap opens.

Figure 6 shows the displacement of the cone as a function of the impurity depth  $z_0$ . As in Figure 2, a shift of the Dirac cone as the impurity is placed deeper is observed, in opposition to hole doping [17]. While DFT calculations are difficult to address due to their computational cost when the impurity is far from the surface, this minimal model allows us to predict a return to the pristine case for large  $z_0$ . Despite the aforementioned limitations, the model describes qualitatively well the phenomenon and it can be used as a simple approach to the effect of the impurity on the surface bands.

### B. Green's function approach

In the previous subsection, the interaction of the electron with the impurity was assumed weak so that the

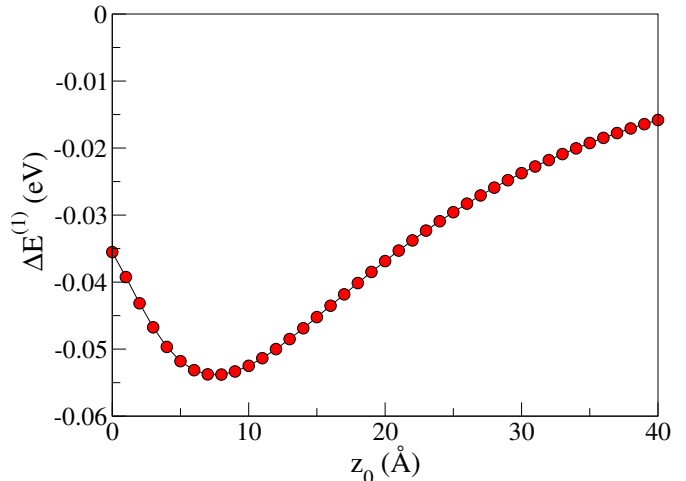


FIG. 6. Displacement of the Dirac cone in energy  $\Delta E^{(1)}$  as a function of the impurity depth  $z_0$ , obtained from PT calculations.

first-order perturbation theory was a reasonable approximation. We can go beyond this limit, summing up all terms of the perturbation series by means of the Green's function approach. To this end, we start with Eq. (1) and neglect the quadratic in momentum term ( $B = 0$ ). The linear approximation (Dirac-like equation) is unable to explain the existence of surface states in a topological insulator unless a normal semiconductor is attached, thus forming a heterojunction. In this way, there exists a band inversion along the direction normal to the surface and interface states can appear (see, e.g., Ref. [28] and references therein).

The envelope functions of the electron states near the band extrema are then determined from the following Dirac-like Hamiltonian

$$\mathcal{H}_0 = v \boldsymbol{\alpha} \cdot \mathbf{k} + m(z) \beta, \quad (5)$$

where we assume aligned and same-sized gaps for simplicity. The origin of energy is set at the center of the gaps ( $\epsilon = 0$ ) and the mass term is given as  $m(z) = m \text{sign}(z)$ . The Hamiltonian (5) acts upon the envelope function  $\boldsymbol{\chi}(\mathbf{r})$ , which is a four-component vector composed of the two-component spinors  $\boldsymbol{\chi}_+(\mathbf{r})$  and  $\boldsymbol{\chi}_-(\mathbf{r})$ . Its  $z$ -component decays as  $\sim \exp(-|z|/d)$ , with  $d = v/\Delta$ , and the interface dispersion relation is a single Dirac cone  $E(\mathbf{k}_{\parallel}) = \pm v|\mathbf{k}_{\parallel}|$ .

The presence of the impurity, located at  $\mathbf{r}_0 = (0, 0, z_0)$  without loss of generality, breaks the translational symmetry in the surface and the in-plane momentum is no longer conserved. Expressing distance in units of  $d$  and energy in units of  $m$ , the Dirac-like equation for the en-

velope function can be cast in the form

$$\left[ E\mathbb{1}_4 + i\alpha_z \frac{\partial}{\partial z} + i\boldsymbol{\alpha}_{\parallel} \cdot \nabla_{\parallel} - \beta \text{sign}(z) - V(\mathbf{r} - \mathbf{r}_0)\mathbb{1}_4 \right] \chi(\mathbf{r}) = \mathbf{0}. \quad (6)$$

The actual interaction potential  $V(\mathbf{r} - \mathbf{r}_0)$  will be replaced by a non-local separable potential of the form

$$V(\mathbf{r} - \mathbf{r}_0)\chi(\mathbf{r}) \longrightarrow \lambda\omega(\mathbf{r} - \mathbf{r}_0) \int d^3\mathbf{r}'\omega(\mathbf{r}' - \mathbf{r}_0)\chi(\mathbf{r}'), \quad (7)$$

where  $\lambda$  is a coupling constant and  $\omega(\mathbf{r} - \mathbf{r}_0)$  is a real function referred to as shape function hereafter. It is worth mentioning that this replacement is exact, in the sense that it is always possible to find a non-local separable potential (or a sum of them) able to reproduce any set of given electronic states and, consequently, there is no theoretical limitation to the numerical accuracy with which physical results can be obtained [36]. In spite of its seemingly more complicated form, equation (7) is amenable to analytical solution for any arbitrary shape function. Therefore, one can test different shape functions until the desired accuracy of the results is obtained. Typically naive functions with very few adjustable parameters are good candidates [37–42].

The Green's function for the unperturbed problem ( $\lambda = 0$ ) and the Green's function for the total Hamiltonian in terms of the transition operator are derived in Appendix C. Poles in the complex plane of the transition matrix  $E = E_r - i\Gamma$ , where  $E_r$  and  $\Gamma$  are real magnitudes, yield the energies of the impurity states. Resonances within the gap are given by the condition  $|E_r| < 1$ . According to the impurity model presented, an impurity embedded in a bulk semiconductor can support a truly bound state. Straightforward calculations lead to the following energy for the bound state

$$E_b = \text{sign}(\lambda) \left( 1 - \frac{4\pi}{|\lambda|k_c} \right). \quad (8)$$

Since only states within the gap correspond to bound states in this model ( $|E_b| < 1$ ), there exists a minimum value of the product  $|\lambda|k_c$  to induce bound states. If  $|\lambda|k_c < 2\pi$  the impurity cannot bind electrons ( $\lambda < 0$ ) or holes ( $\lambda > 0$ ) in bulk semiconductors.

Figure 7 shows the real and imaginary parts of the poles of the transition matrix as a function of the position of the impurity when  $k_c = 100$  and  $\lambda = -0.15$ . The real part  $E_r$  approaches the value in the bulk material  $E_b$  when increasing  $z_0$ , as expected. These impurity states move to higher energies as the distance from the surface increases, as in Ref. [43]. The alternating behavior found in DFT calculations, with different energy shifts of the impurity bands for even (odd) slabs, is not reflected in this model since simpler, exponentially-decaying wavefunctions are used here.

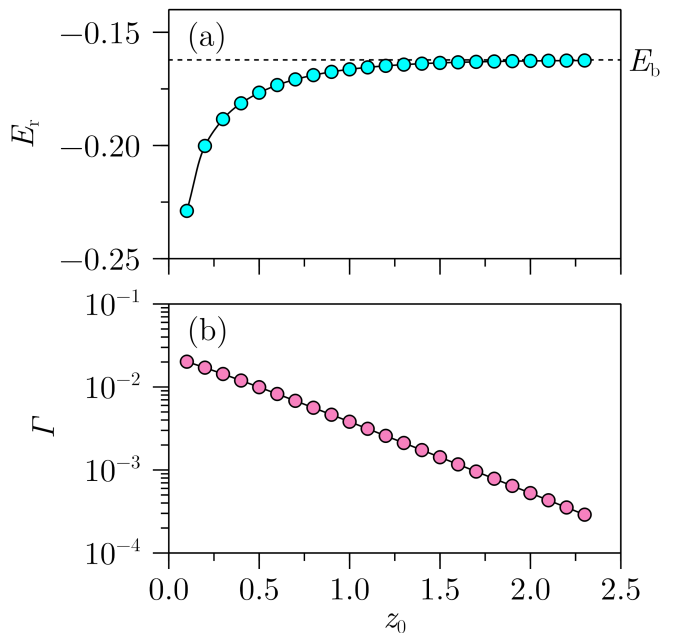


FIG. 7. Real and imaginary parts of the complex poles  $E = E_r - i\Gamma$  of the transition matrix as a function of the impurity position. The parameters of the interaction potential are  $\lambda = -0.15$  and  $k_c = 100$ . Dashed line indicates the energy of the impurity bound state in the bulk semiconductor [see equation (8)].

#### IV. CONCLUSIONS

Doping a SnTe slab with a non-magnetic Sb impurity breaks mirror symmetry, which affects the well-known topologically-protected surface states of pristine SnTe. Additionally, impurity doping has an effect on the band structure: it creates new impurity bands which hybridize with the aforementioned surface states. We have studied this doped system by resorting to first-principles calculations and continuum models. DFT calculations have been performed to study a finite structure, i.e., a slab with two surfaces, as well as a semi-infinite geometry with only one surface. We have analyzed the role of crystal symmetries for each case. Surface states are unaltered when a single substitutional impurity is used in a semi-infinite system, yielding a band structure with Dirac cones as well as spin-polarized impurity states. In contrast, a slab geometry even with 16 atomic layers presents coupling of states at opposite surfaces, which produces a small gap in the Dirac cones. Our calculations allow us to isolate the contribution of either the impurity or the first atomic layers of the surface to the electronic structure of the system, which is specially useful since we consider different impurity positions. Impurity states show an interesting alternating behavior depending on the location of the impurity inside the material, which can be regarded as an even-odd effect.

A continuum Hamiltonian is also used to describe the

effect of doping on the Dirac cone, which shifts downwards. This result coincides qualitatively with our DFT calculations and allows us to predict the behavior of the system when the impurity is placed deeper in the slab. As for the hybridization between the topologically-protected surface states and the impurity states, a simplified version of the aforementioned Hamiltonian is used, showing a diminishing resonance as the impurity moves inwards.

SnTe, the first discovered topological crystalline insulator, is an excellent platform to explore the interplay of symmetry and topology in this class of Dirac matter. A simple perturbation such as a substitutional impurity is shown to give rise to non-trivial spin textures; besides its fundamental interest, tuning the Dirac cones of topological insulators can be of interest for transport and spintronic applications.

## V. ACKNOWLEDGMENTS

We thank Gloria Platero for generously sharing her computational resources and Sergio Bravo for helpful discussions. This work was supported by Ministerio de Economía y Competitividad, Spanish MCIU and AEI and the European Union under Grants PGC2018-097018-B-I00 (MCIU/AEI/FEDER, UE) and PID2019-106820RB-C21.

### Appendix A: Additional DFT results

A more detailed analysis of the spin texture of pristine and impurity-doped SnTe is illustrated by the following figures. Fig. A.1 depicts PDOS( $k_x, k_y$ ) and spin texture maps of SnTe above the Dirac cone. Two pairs of Dirac cones appear, which are later folded into a x-shaped four-fold pattern at  $\Gamma$ . The rightmost panel illustrates the absence of out-of-plane spin texture.

Fig. A.2 shows the persistence of the pristine SnTe spin texture as impurities are included. As mentioned in Fig. 3, the helicity is unaltered independently of the impurity position. As can be seen in Fig. 4, the spin texture changes sign upon moving above or below the Dirac cone.

### Appendix B: Surface states in the quadratic Dirac equation

The surface states used in the analytic calculations are obtained considering a semi-infinite slab extended for  $z > 0$  and with periodic boundary conditions in the  $x$ - and  $y$ -directions. DFT calculations use a periodical supercell of size  $L_x \times L_y$ ; in order to match the same conditions of the *ab-initio* structure we consider periodic boundary conditions in  $x$ - and  $y$ -directions while the  $z$  coordinate is unbounded in performing the integrals of Eq. (4).

Due to the breaking of translational symmetry, we solve the Hamiltonian (3) with the Peierls substitution  $k_z \rightarrow -i\partial_z$ , using the *ansatz* of the form

$$\psi \sim e^{-\lambda z} \exp[i(k_x x + k_y y)]\Phi ; \quad (\text{B1})$$

in other words, we assumed plane waves in the in-plane directions, an exponentially decay form in the  $z$ -direction and a constant spinorial part  $\Phi$ .

We found that two decay lengths satisfy the eigenvalue equation:

$$\lambda_{1,2} = \frac{v}{2|B|} \left( 1 \pm \sqrt{1 - \frac{4m|B|}{v^2} + \frac{4B^2 k_{\parallel}^2}{v^2}} \right). \quad (\text{B2})$$

By combining solutions of the form (B1) in order to fulfill the hard-wall boundary conditions at  $z = 0$ , we obtain two surface states solutions with linearly dispersive energy given by  $E_{\pm} = \epsilon \pm v k_{\parallel} \text{sign}(B)$  with wavefunctions

$$\psi_+ = A_s (e^{-\lambda_1 z} - e^{-\lambda_2 z}) \exp[i(k_x x + k_y y)]\Phi_+^0, \quad (\text{B3})$$

$$\psi_- = A_s (e^{-\lambda_1 z} - e^{-\lambda_2 z}) \exp[i(k_x x + k_y y)]\Phi_-^0, \quad (\text{B4})$$

where  $\Phi_{\pm}^0$  are space-independent normalized spinors and the normalization constant depends on the momenta and model parameters:

$$A_s = \frac{1}{\sqrt{L_x L_y}} \sqrt{\frac{2\lambda_1 \lambda_2 (\lambda_1 + \lambda_2)}{(\lambda_1 - \lambda_2)^2}}. \quad (\text{B5})$$

The numerical value of the parameters have been obtained by fitting to DFT data and are reported in Table I.

SnTe
$\epsilon = -0.065 \text{ eV}$
$m = 0.07 \text{ eV}$
$v = 1.591 \text{ eV \AA}$
$B = 2.74 \text{ eV \AA}^2$

TABLE I. Parameters of the fit to DFT data.

In Eq. (3), replacing the electron free mass by the effective mass and the vacuum dielectric constant by that of the medium, the following relation can be easily obtained:

$$R_y^* a_B^* = R_y a_B / \epsilon_r, \quad (\text{B6})$$

where  $R_y$  and  $a_B$  are the well-known hydrogen Rydberg energy and Bohr radius and  $\epsilon_r$  is the relative permittivity. The value of the permittivity in SnTe has been tabulated in multiple references [44, 45] for a wide range of temperatures. In our DFT simulations, as already mentioned in the previous sections, we are in a room-temperature regime; hence, the tabulated value of  $\epsilon \approx 40$  at room temperature is the more convenient [44, 46].



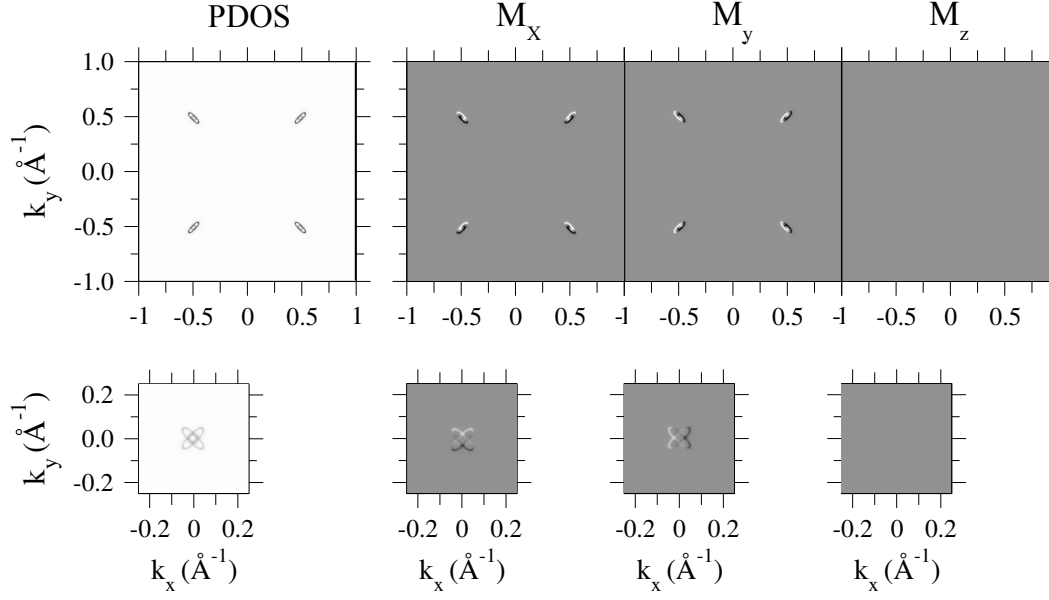


FIG. A.1. PDOS( $k_x, k_y$ ) (left panel) and maps of the magnetization components  $M_x(k_x, k_y)$ ,  $M_y(k_x, k_y)$  and  $M_z(k_x, k_y)$  of pristine SnTe at 0.05 eV. Top panel: unfolded  $1 \times 1$  unit cell, four helical edge states appear. Bottom panel:  $c(4 \times 4)$  folded unit cell, the previous helical states arrange around  $\Gamma$  in a fourfold pattern. White and black shades account for positive and negative values of  $M_i$ , respectively.

### Appendix C: Green's function in the absence of impurity

When describing the envelope function  $\chi(\mathbf{r})$ , the momentum perpendicular to the growth direction  $\mathbf{k}_{\parallel}$  is conserved and the envelope function can be factorized as  $\chi(\mathbf{r}) = \tilde{\chi}(z) \exp(i\mathbf{r}_{\parallel} \cdot \mathbf{k}_{\parallel})$ . It is understood that the subscript  $\parallel$  in a vector indicates the nullification of its  $z$ -component, namely  $\mathbf{r}_{\parallel} = (x, y, 0)$  and  $\mathbf{k}_{\parallel} = (k_x, k_y, 0)$ . It is found that  $\tilde{\chi}(z) \sim \exp(-|z|/d)$ , with  $d = v/\Delta$ .

The Green's function for the unperturbed problem ( $\lambda = 0$ ) satisfies the following equation:

$$\left[ E\mathbb{1}_4 + i\alpha_z \frac{\partial}{\partial z} + i\boldsymbol{\alpha}_{\parallel} \cdot \nabla_{\parallel} - \beta \text{sign}(z) \right] G_0(\mathbf{r}, \mathbf{r}'; E) = \delta(\mathbf{r} - \mathbf{r}')\mathbb{1}_4. \quad (\text{C1})$$

The Green's function  $G_0(\mathbf{r}, \mathbf{r}'; E) = \langle \mathbf{r} | \hat{G}_0(E) | \mathbf{r}' \rangle$  is the matrix element of the unperturbed resolvent  $\hat{G}_0(E)$  in coordinate representation.

Let  $\hat{G}(E)$  be the resolvent of the Hamiltonian  $\hat{H}_0 + \hat{V}$ , where  $\hat{V} = |\omega\rangle\lambda\langle\omega|$  is the operator associated to the non-local separable potential (7).  $\hat{G}(E)$  and  $\hat{G}_0(E)$  are related by the well-known equation  $\hat{G}(E) = \hat{G}_0(E) + \hat{G}_0(E)\hat{T}(E)\hat{G}_0(E)$  (see Ref. [47]), where

$$\hat{T}(E) = \left[ \mathbb{1} - \hat{V}\hat{G}_0(E) \right]^{-1} \hat{V}, \quad (\text{C2})$$

is the transition operator. A pole of  $\hat{T}(E)$  at a real/complex energy  $E$  corresponds to a

bound/resonance state. After some lengthy but straightforward algebra we get the following transcendental equation for the poles of the transition operator  $\hat{T}(E)$

$$\det[\mathbb{1}_4 - \lambda \int d^3\mathbf{r} \int d^3\mathbf{r}' G_0(\mathbf{r}, \mathbf{r}'; E) \omega(\mathbf{r} - \mathbf{r}_0) \omega(\mathbf{r}' - \mathbf{r}_0)] = 0, \quad (\text{C3})$$

where  $G_0(\mathbf{r}, \mathbf{r}'; E)$  can be expanded as

$$G_0(\mathbf{r}, \mathbf{r}'; E) = \frac{1}{4\pi^2} \int d^2\mathbf{k}_{\parallel} G_0(z, z'; \mathbf{k}_{\parallel}; E) \exp[i\mathbf{k}_{\parallel} \cdot (\mathbf{r}_{\parallel} - \mathbf{r}'_{\parallel})]. \quad (\text{C4})$$

with

$$G_0(z, z'; \mathbf{k}_{\parallel}; E) = \frac{e^{-\kappa|z-z'|}}{2\kappa} [i\kappa\alpha_z \text{sign}(z-z') + \beta \text{sign}(z) + E\mathbb{1}_4] + \frac{e^{-\kappa(|z|+|z'|)}}{2\kappa(E^2 - k_{\parallel}^2)} \left( i\alpha_z\beta + \frac{1}{\kappa} \mathbb{1}_4 \right) [i\kappa\alpha_z \text{sign}(z) + \beta \text{sign}(z) + E\mathbb{1}_4], \quad (\text{C5})$$

and  $\kappa^2 = 1 + k_{\parallel}^2 - E^2$ .

The proper Green's function of the unperturbed band-inverted heterojunction can be obtained as follows. We introduce (C4) in equation (C1) to obtain

$$\left[ E\mathbb{1}_4 - \hat{h}_0(z) \right] G_0(z, z'; \mathbf{k}_{\parallel}; E) = \delta(z - z')\mathbb{1}_4, \quad \hat{h}_0(z) \equiv -i\alpha_z \frac{\partial}{\partial z} + \boldsymbol{\alpha}_{\parallel} \cdot \mathbf{k}_{\parallel} + \beta \text{sign}(z). \quad (\text{C6})$$

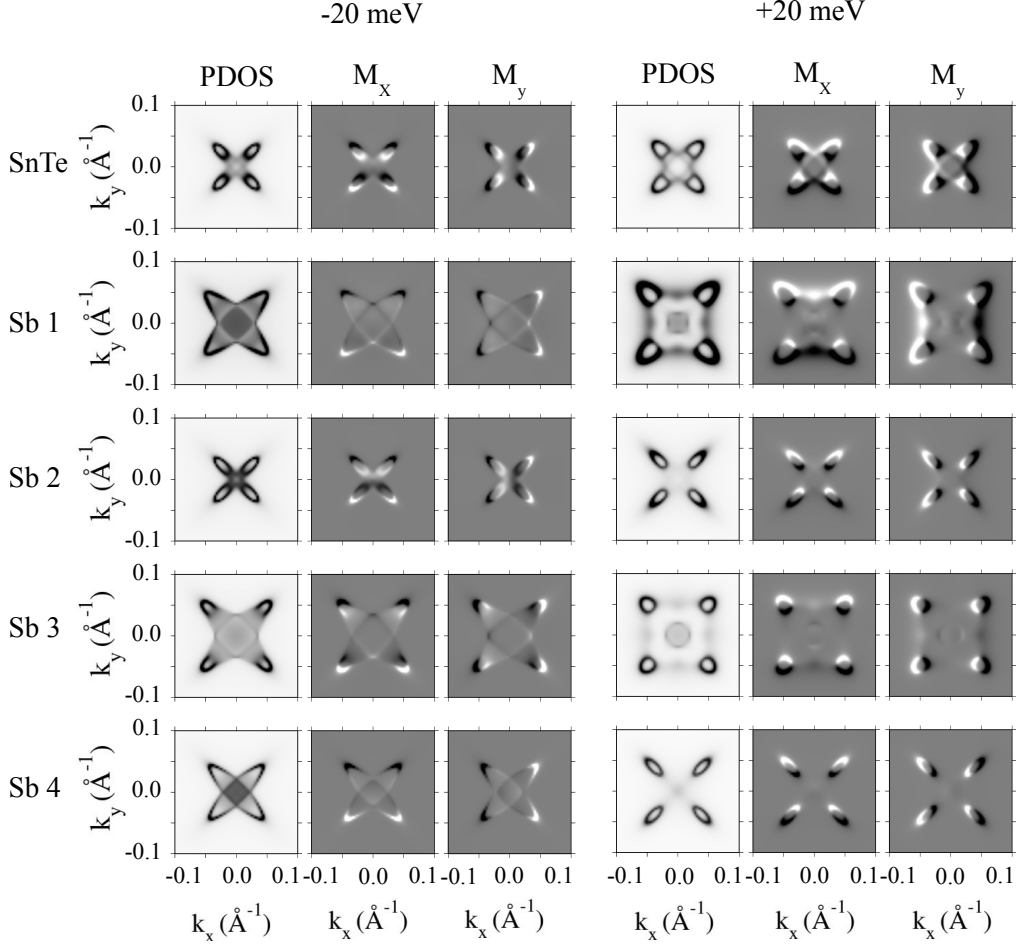


FIG. A.2. PDOS( $k_x, k_y$ ) (left panel) and maps of the magnetization components  $M_x(k_x, k_y)$  and  $M_y(k_x, k_y)$  at 20 meV below (left panels) and above (right panels) the Dirac point. White and black shades account for positive and negative values of  $M_i$ , respectively.

The resolvent of  $\hat{h}_0$  is  $\hat{G}_0(E) = (E\mathbb{1}_4 - \hat{h}_0)^{-1}$ . We now define the auxiliary resolvent  $\hat{g}_0(E) = (E^2\mathbb{1}_4 - \hat{h}_0^2)^{-1}$  so that  $\hat{G}_0(E) = (E\mathbb{1}_4 + \hat{h}_0)\hat{g}_0(E)$ . Therefore, once  $\hat{g}_0(E)$  is known, we can easily obtain  $\hat{G}_0(E)$ . In coordinate representation

$$\left[ \left( \frac{\partial^2}{\partial z^2} - \kappa^2 \right) \mathbb{1}_4 - 2i\beta\alpha_z\delta(z) \right] g_0(z, z'; \mathbf{k}_{\parallel}; E) = \delta(z - z')\mathbb{1}_4, \quad (\text{C7})$$

with  $\kappa^2 = 1 + k_{\parallel}^2 - E^2$ . This equation can be easily solved regarding the term  $-2i\beta\alpha_x\delta(x)$  as an interaction potential and then using the Dyson equation

$$g_0(z, z'; \mathbf{k}_{\parallel}; E) = -\frac{1}{2\kappa} e^{-\kappa|z-z'|}\mathbb{1}_4 + \frac{e^{-\kappa(|z|+|z'|)}}{2(E^2 - k_{\parallel}^2)} \left( i\beta\alpha_z + \frac{1}{\kappa} \mathbb{1}_4 \right). \quad (\text{C8})$$

Finally, recalling that  $\hat{G}_0(E) = (E + \hat{h}_0)\hat{g}_0(E)$ , we get equation (C5).

Once the basic equations are presented, we now need to take a particular shape function to perform the calculation. In what follows we consider

$$\omega(\mathbf{r} - \mathbf{r}_0) = f(z - z_0)\delta(\mathbf{r}_{\parallel}), \quad (\text{C9})$$

where  $f(z)$  is a top-hat function of width  $L$  and height  $1/L$ , centered at  $z_0$  and approaching the  $\delta$ -function limit ( $L \ll 1$ ). The transcendental equation (C3) for the poles reduces to

$$\det[\mathbb{1}_4 - M(E)] = 0, \quad (\text{C10a})$$

$$M(E) \equiv \frac{\lambda}{4\pi^2} \int d^2\mathbf{k}_{\parallel} \int dz \int dz' f(z - z_0)f(z' - z_0) G_0(z, z'; \mathbf{k}_{\parallel}; E). \quad (\text{C10b})$$

We have numerically solved equation (C10a) considering a finite bandwidth. This is equivalent to introduce an

upper cutoff for the in-plane momentum,  $k_c$ . In this way, we prevent divergences when taking the limit  $L \rightarrow 0$ , i.e.  $f(z - z_0) \rightarrow \delta(z - z_0)$ .

## REFERENCES

- 
- [1] Hasan M Z and Kane C L 2010 *Reviews of Modern Physics* **82** 3045–3067
- [2] Qi X L and Zhang S C 2011 *Rev. Mod. Phys.* **83**(4) 1057–1110
- [3] Manchon A, Koo H C, Nitta J, Frolov S M and Duine R A 2015 *Nat. Mater.* **14** 871–882
- [4] Ando Y and Fu L 2015 *Annual Review of Condensed Matter Physics* **6** 361–381
- [5] Hsieh T H, Lin H, Liu J, Duan W, Bansil A and Fu L 2012 *Nat. Commun.* **3** 982
- [6] Dziawa P, Kowalski B J, Dybko K, Buczko R, Szczerbakow A, Szot M, Łusakowska E, Balasubramanian T, Wojek B M, Berntsen M H, Tjernberg O and Story T 2012 *Nature Materials* **11** 1023–1027
- [7] Tanaka Y, Ren Z, Sato T, Nakayama K, Souma S, Takahashi T, Segawa K and Ando Y 2012 *Nature Physics* **8** 800–803
- [8] Xu S Y, Liu C, Alidoust N, Neupane M, Qian D, Belopolski I, Denlinger J, Wang Y, Lin H, Wray L a *et al.* 2012 *Nat. Commun.* **3** 1–11
- [9] Okada Y, Serbyn M, Lin H, Walkup D, Zhou W, Dhital C, Neupane M, Xu S, Wang Y J, Sankar R, Chou F, Bansil A, Hasan M Z, Wilson S D, Fu L and Madhavan V 2013 *Science* **341** 1496–1499
- [10] Schindler F, Cook A M, Vergniory M G, Wang Z, Parkin S S P, Bernevig B A and Neupert T 2018 *Sci. Adv.* **4** eaat0346
- [11] Dimmock J O, Melngailis I and Strauss A J 1966 *Phys. Rev. Lett.* **16**(26) 1193–1196
- [12] Ozawa H, Yamakage A, Sato M and Tanaka Y 2014 *Phys. Rev. B* **90** 045309
- [13] Liu J, Hsieh T H, Wei P, Duan W, Moodera J and Fu L 2013 *Nature Materials* **13** 178–183
- [14] Araújo A L, Ferreira G J and Schmidt T M 2018 *Sci. Rep.* **8** 9452
- [15] Hoang K, Mahanti S D and Kanatzidis M G 2010 *Phys. Rev. B* **81** 115106
- [16] Zhao X, Zhang X, Wang T, Xia C and Wei S 2018 *Journal of Materials Science* **53** 15995–16000
- [17] Schmidt T M and Srivastava G 2020 *Computational Materials Science* **182** 109777
- [18] Yarmohammadi M and Mirabbaszadeh K 2019 *Physical Chemistry Chemical Physics* **21** 21633–21650
- [19] Fang C, Gilbert M J and Bernevig B A 2014 *Phys. Rev. Lett.* **112**(4) 046801
- [20] Hoa L T, Phong T C and Hoi B D 2020 *Phys. Chem. Chem. Phys.* **22**(24) 13613–13621
- [21] Hulm J K, Jones C K, Deis D W, Fairbank H A and Lawless P A 1968 *Phys. Rev.* **169**(2) 388–394
- [22] Soler J M, Artacho E, Gale J D, García A, Junquera J, Ordejón P and Sánchez-Portal D 2002 *J. Phys. Condens. Matter* **14** 2745
- [23] Perdew J P, Burke K and Ernzerhof M 1996 *Phys. Rev. Lett.* **77** 3865
- [24] Cuadrado R and Cerdá J I 2012 *Journal of Physics: Condensed Matter* **24** 086005
- [25] Cerdá J, Van Hove M A, Sautet P and Salmeron M 1997 *Phys. Rev. B* **56**(24) 15885
- [26] Rossen E T R, Flipse C F J and Cerdá J I 2013 *Phys. Rev. B* **87**(23) 235412
- [27] Wang Y J, Tsai W F, Lin H, Xu S Y, Neupane M, Hasan M Z and Bansil A 2013 *Phys. Rev. B* **87** 235317
- [28] Shen S 2017 *Topological Insulators: Dirac Equation in Condensed Matter* (Berlin: Springer)
- [29] Liu C X, Qi X L, Zhang H, Dai X, Fang Z and Zhang S C 2010 *Phys. Rev. B* **82** 045122
- [30] Shen S Q, Shan W Y and Lu H Z 2010 *SPIN* **1** 33
- [31] Zhang H, Liu C X, Qi X L, Dai X, Fang Z and Zhang S C 2009 *Nat. Phys.* **5** 438
- [32] Zhang F, Kane C L and Mele E J 2012 *Phys. Rev. B* **86** 081303
- [33] Liu J, Duan W and Fu L 2013 *Phys. Rev. B* **88** 241303
- [34] Knox R 1963 *Theory of excitons* (Cambridge: Academic Press)
- [35] Ibach H and Lüth H 2009 *Solid-State Physics: An Introduction to Principles of Materials Science* (Springer)
- [36] Glasser M 1977 *Surf. Sci.* **64** 141
- [37] Knight B W and Peterson G A 1963 *Phys. Rev.* **132** 1085
- [38] Sievert P R and Glasser M L 1973 *Phys. Rev. B* **7** 1265
- [39] López S and Domínguez-Adame F 2002 *Semicon. Sci. Technol.* **17** 227
- [40] Domínguez-Adame F, Méndez B, Maciá E and González M A 1991 *Mol. Phys.* **74** 1065
- [41] Domínguez-Adame F, Diez E and Sánchez A 1995 *Phys. Rev. B* **51** 8115
- [42] González-Santander C, Apostolova T and Domínguez-Adame F 2013 *J. Phys. Condens. Matter* **25** 335802
- [43] Kantser V G and Malkova N M 1994 *Phys. Rev. B* **50**(23) 17074–17079
- [44] Riedl H, Dixon J and Schoolar R 1965 *Solid State Commun.* **3** 323
- [45] Cardona M 1965 *J. Appl. Phys.* **36** 2181
- [46] Adachi S 1999 *Optical Constants of Crystalline and Amorphous Semiconductors: Numerical Data and Graphical Information* (Berlin: Springer)
- [47] Economou E N 2006 *Green's functions in quantum physics* (Berlin: Springer)